

NUMERICAL INTEGRATION OF NON-LINEAR ELASTIC MULTI-BODY SYSTEMS

O. A. BAUCHAU,* G. DAMILANO AND N. J. THERON

*Rensselaer Polytechnic Institute, J.E.C. 4018, 110, 8th Street, Department of Mechanical Engineering,
Aeronautical Engineering and Mechanics, Troy, NY, 12180, U.S.A.*

SUMMARY

This paper is concerned with the modelling of nonlinear elastic multi-body systems discretized using the finite element method. The formulation uses Cartesian co-ordinates to represent the position of each elastic body with respect to a single inertial frame. The kinematic constraints among the various bodies of the system are enforced via the Lagrange multiplier technique. The resulting equations of motion are stiff, non-linear, differential-algebraic equations. The integration of these equations presents a real challenge as most available techniques are either numerically unstable, or present undesirable high frequency oscillations of a purely numerical origin. An approach is proposed in which the equations of motion are discretized so that they imply conservation of the total energy for the elastic components of the system, whereas the forces of constraint are discretized so that the work they perform vanishes exactly. The combination of these two features of the discretization guarantees the stability of the numerical integration process for non-linear elastic multi-body systems. Examples of the procedure are presented.

KEY WORDS: multi-body systems; dynamic analysis

1. INTRODUCTION

Multi-body systems can be broadly categorized into three problem types: multi-body systems consisting of a collection of rigid bodies in arbitrary motion with respect to each other; systems consisting of a collection of elastic bodies where the elastic displacements and rotations with respect to a body attached frame of reference are small; and finally systems consisting of a number of elastic bodies where elastic displacements and rotations can be arbitrarily large. The analysis methodologies that are optimum for each category vary widely.

This paper is concerned with the analysis of non-linear elastic multi-body systems, i.e. a collection of bodies in arbitrary motion with respect to each other while each body is undergoing large displacements and rotations with respect to a body attached frame of reference. The focus is on problems where the strains within each elastic body remain small.

Each elastic body is modelled using the finite element method. The use of beam elements will be demonstrated in this work. The location of each node is represented by its Cartesian co-ordinates in an inertial frame, and the rotation of the cross-section at each node is represented by a finite rotation tensor expressed in the same inertial frame. The kinematic constraints among the various bodies are enforced via the Lagrange multiplier technique. Though this approach does not involve the minimum set of co-ordinates,¹ it allows a modular development of finite elements for the enforcement of the kinematic constraints. The representation of the displacements and rotation quantities in a single inertial frame remarkably simplifies the expression for the kinetic energy, as demonstrated by Simo and Vu-Quoc.²

The equations of motion resulting from the modelling of multi-body systems with the above methodology presents distinguishing features: they are stiff, non-linear, differential-algebraic equations. The stiffness of the system stems not only from the presence of high frequencies in the elastic members, but also from the infinite frequencies associated with the kinematic constraints. Indeed, no mass is associated with the Lagrange multipliers giving rise to algebraic equations coupled to the other equations of the system which are differential in nature.

The time integration of the resulting equations of motion give rise to a number of problems such as numerical instabilities and high frequency oscillations of a purely numerical origin. A thorough review of time integration schemes used in structural dynamics is found in Reference 3. The Newmark scheme⁴ is a widely used scheme to integrate the equations of motion resulting from finite element discretizations. Cardona and Geradin⁵ have shown that this scheme presents a weak instability when applied to constrained multi-body systems. The culprit is the presence of algebraic equations which are equivalent to infinite frequencies.

The Hilber-Hughes-Taylor (HHT)⁶ scheme was introduced to eliminate the high frequency oscillations of a purely numerical origin resulting from the use of the Newmark scheme for large finite element problems. Indeed, larger and larger finite element models present higher and higher frequencies which in turn generate high frequency oscillations. The HHT scheme alleviates this problem by introducing high frequency numerical dissipation. Cardona and Geradin⁵ have shown that the use of the HHT scheme in constrained multi-body problems can yield satisfactory system response. Numerical oscillations are observed in the time history response of accelerations, Lagrange multipliers, and velocities, though to a lesser extent. However, these high frequency oscillations are rapidly damped out. As the complexity of the constrained multi-body system increases, an increasing amount of numerical dissipation is required to avoid numerical instabilities and high frequency oscillations.

A more recent study by Farhat *et al.*⁷ explores various approaches for constructing HHT based, penalty-free, unconditionally stable algorithms for constrained systems. For all these

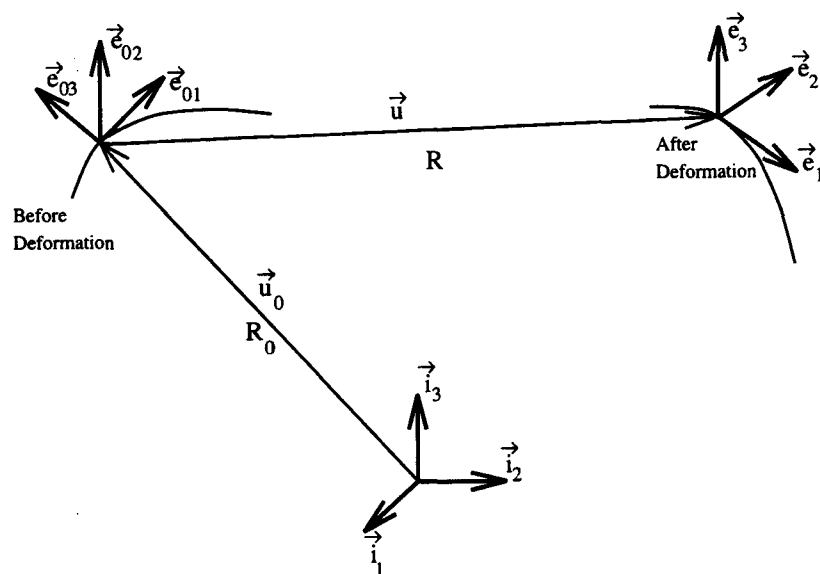


Figure 1. Beam reference line in undeformed and deformed position

studies, stability proofs are derived for linear systems, then the resulting algorithms are applied to non-linear problem.

Though this approach is satisfactory, numerical oscillations are never completely eliminated. However, it raises a basic question: why introduce numerical dissipation to control the weak instability inherent to the Newmark scheme in the presence of infinite frequencies, rather than using a scheme that behaves adequately in the presence of such frequencies? This paper investigates an alternative integration scheme for constrained, non-linear elastic multi-body systems. The focus is to provide a formal proof of stability for non-linear, constrained multi-body system.

An energy preserving scheme is derived for integration of beam equations. The algorithm presented here is similar to the energy preserving algorithms presented by Simo and Wong⁸ for rigid body dynamics, and by Simo and Tarnow⁹ for elastodynamics. The forces of constraint associated with kinematic constraints will be discretized in such a way that they perform no work. These two features, energy preservation for elastic elements, and vanishing work of the constraint forces, result in preservation of the total energy of the multi-body system, and numerical stability of the integration process is then guaranteed.³

The non-linear beam equations and the energy preserving scheme are derived in Section 2. Section 3 describes the discretization of the forces of constraint corresponding to a revolute joint. Several numerical examples are presented in Section 4. Conclusions and recommendations for future work are presented in the last section.

2. EQUATIONS OF MOTION OF BEAM MODELS

Let \hat{i}_1, \hat{i}_2 , and \hat{i}_3 form an inertial triad denoted \mathcal{S} ; $\hat{e}_{01}, \hat{e}_{02}$ and \hat{e}_{03} be a triad denoted \mathcal{S}_0 attached to the reference line of the beam before deformation; and \hat{e}_1, \hat{e}_2 and \hat{e}_3 a triad denoted \mathcal{S}^* attached to the reference line of the beam after deformation. The planes formed by $\hat{e}_{02}, \hat{e}_{03}$, and \hat{e}_2, \hat{e}_3 define the plane of the cross-section of the beam before, and after deformation, respectively (see Figure 1).

The strain energy of the beam is written as:

$$V = \frac{1}{2} \int_0^L \underline{e}^{*\text{T}} C^* \underline{e}^* dx_1 \quad (1)$$

where L is the length of the beam and x_1 the curvilinear coordinate along the reference line. C^* are the components of the sectional stiffness tensor and \underline{e}^* the components of the sectional strain vector, both measured in \mathcal{S}^* . These sectional strains are related to the sectional displacements as

$$\underline{e}^* = \begin{bmatrix} \underline{\varepsilon}^* \\ \underline{k}^* \end{bmatrix} = \mathcal{R}^T \underline{e} = \mathcal{R}^T \begin{bmatrix} \underline{\varepsilon} \\ \underline{k} \end{bmatrix} = \mathcal{R}^T \begin{bmatrix} (\underline{u}'_0 + \underline{u}') - RR_0 \underline{1} \\ \underline{k} \end{bmatrix} \quad (2)$$

where

$$\mathcal{R} = \begin{bmatrix} RR_0 & 0 \\ 0 & RR_0 \end{bmatrix} \quad (3)$$

and $\underline{1}^T = [1 \ 0 \ 0]$. The following quantities are all measured in \mathcal{S} : R_0 defines the components of the rotation tensor from \mathcal{S} to \mathcal{S}_0 ; R the components of the rotation tensor from \mathcal{S}_0 to \mathcal{S}^* ; \underline{u}_0 the components of the position vector of a point on the reference line before deformation; \underline{u} the components of the displacement vector of the deformed reference line with respect to the undeformed configuration; and \underline{k} the components of the sectional elastic curvature vector, with

$\tilde{k} = R'R^T$. The notation $(\cdot)'$ is used to denote a derivative with respect to x_1 , and $(\tilde{\cdot})$ denotes a skew-symmetric matrix.

The kinetic energy of the beam is expressed as:

$$K = \frac{1}{2} \int_0^L \underline{v}^{*\text{T}} M^* \underline{v}^* dx_1 \quad (4)$$

where M^* are the components of the sectional inertia tensor, and \underline{v}^* the components of the sectional velocity vector, both measured in \mathcal{S}^* . These sectional velocities are related to the sectional displacements as

$$\underline{v}^* = \mathcal{R}^T \underline{v} = \mathcal{R}^T \begin{bmatrix} \dot{\underline{u}} \\ \underline{\omega} \end{bmatrix} \quad (5)$$

where $\underline{\omega}$ are the components of the sectional angular velocity, with $\tilde{\omega} = \dot{R}R^T$; and a superposed dot denotes derivative with respect to time.

Virtual variations in sectional strains and velocities result in:

$$\delta \underline{e}^{*\text{T}} = \underline{\delta d}^T \mathcal{R} + \underline{\delta d}^T \mathcal{U} [(\tilde{u}'_0 + \tilde{u}')^T] \mathcal{R} \quad (6)$$

and

$$\delta \underline{v}^{*\text{T}} = \underline{\delta d}^T \mathcal{R} + \underline{\delta d}^T \mathcal{U} [\tilde{u}'^T] \mathcal{R} \quad (7)$$

where $\underline{\delta d}^T = (\delta \underline{u}^T, \delta \underline{\psi}^T)$ are the virtual displacements and rotations measured in \mathcal{S} . The virtual rotation is defined as $\tilde{\delta \psi} = \delta R R^T$, and

$$\mathcal{U}[\cdot] = \begin{bmatrix} 0 & 0 \\ [\cdot] & 0 \end{bmatrix} \quad (8)$$

The equations of motion of the beam can be obtained from Hamilton's Principle that states:

$$\int_{t_1}^{t_2} (\delta K - \delta V + \delta W) dt = 0 \quad (9)$$

where δW is the virtual work done by the externally applied forces. Introducing equations (1) and (4) into equation (9) yields

$$\int_{t_1}^{t_2} (\delta \underline{v}^{*\text{T}} M^* \underline{v}^* - \delta \underline{e}^{*\text{T}} C^* \underline{e}^{*\text{T}} + \delta W) dt = 0 \quad (10)$$

Finally, the equations of motion are found by introducing equations (6) and (7) into equation (10), and using the strain, and velocity expressions, (2), and (5), respectively, to find

$$(\mathcal{R} \underline{p}^*) + \mathcal{U}[\tilde{u}'] \mathcal{R} \underline{p}^* - (\mathcal{R} \underline{f}^*)' - \mathcal{U}[\tilde{u}'_0 + \tilde{u}'] \mathcal{R} \underline{f}^* = \underline{q} \quad (11)$$

where the sectional momenta $\underline{p}^* = M^* \underline{v}^*$ and forces $\underline{f}^* = C^* \underline{e}^*$ measured in \mathcal{S}^* were defined. The above equations of motion can be discretized as indicated in Appendix III, equation (36).

An energy preserving integration scheme is obtained by using this discretization across a time step, from t_n to t_{n+1} :

$$\begin{aligned} & \frac{\mathcal{R}_{n+1} p_{n+1}^* - \mathcal{R}_n p_n^*}{\Delta t} + \mathcal{U} \left[\frac{\tilde{u}_{n+1} - \tilde{u}_n}{\Delta t} \frac{2R_{n+1/2} R_0}{4 - a_0} \right] \frac{p_n^* + p_{n+1}^*}{2} \\ & - (\mathcal{Q}_{n+1/2} f_{n+1/2}^*)' - \mathcal{U} \left[\frac{2}{a_0} (\tilde{u}'_0 + \tilde{u}'_{n+1/2}) \right] \mathcal{Q}_{n+1/2} f_{n+1/2}^* = q_{n+1/2} \end{aligned} \quad (12)$$

where \underline{a} are the components of the conformal rotation vector of the rotation from \mathcal{S}_n to \mathcal{S}_{n+1} , measured in \mathcal{S} (see Appendix 1), the subscript $n + 1/2$ refers to the time step mid-point, and $f_{n+1/2}^*$ refers to elastic forces at this mid-point.

In Appendix III, discretization (12) is shown to imply:

$$\int_0^L v_{n+1/2}^{*T} M^* (v_{n+1}^* - v_n^*) + e_{n+1/2}^{*T} C^* (e_{n+1}^* - e_n^*) dx_1 = \Delta W \quad (13)$$

The mid-point sectional velocities and strains are now selected as

$$v_{n+1/2}^* = \frac{v_{n+1}^* + v_n^*}{2}; \quad e_{n+1/2}^* = \frac{e_{n+1}^* + e_n^*}{2} \quad (14)$$

With this choice, equation (13) now becomes

$$E(\underline{u}_{n+1}) - E(\underline{u}_n) = \Delta W \quad (15)$$

where the total energy is defined as $E(\underline{u}) = K + V$. In the absence of externally applied loads (i.e. $\Delta W = 0$), equation (15) implies preservation of the total energy.

3. CONSTRAINT EQUATIONS FOR A REVOLUTE JOINT

Consider two bodies denoted k and l linked at a node by a revolute joint (see Figure 2). In the undeformed configuration, the revolute joint is defined by two coincident triads \mathcal{S}_0^k and \mathcal{S}_0^l with unit vectors $\tilde{e}_{0i}^k = \tilde{e}_{0i}^l$. After deformation, the revolute joint is defined by two distinct triads \mathcal{S}^k and \mathcal{S}^l with unit vectors \tilde{e}_i^k and \tilde{e}_i^l , respectively. Let the rotation matrices from \mathcal{S} to $\mathcal{S}_0^k = \mathcal{S}_0^l$, \mathcal{S}_0^k to \mathcal{S}^k , and \mathcal{S}_0^l to \mathcal{S}^l be R_0 , R^k , and R^l , respectively, all measured in \mathcal{S} . The kinematic constraint corresponding to a revolute joint is the coincidence of \tilde{e}_3^k and \tilde{e}_3^l . This can be written

$$\underline{\mathcal{C}}^T = [\mathcal{C}_1 \quad \mathcal{C}_2 \quad \mathcal{C}_3] = 0 \quad (16)$$

where

$$\mathcal{C}_1 = e_1^{lT} e_3^k, \quad \mathcal{C}_2 = e_2^{lT} e_3^k; \quad \mathcal{C}_3 = (e_1^{kT} e_1^l) \sin \phi + (e_1^{kT} e_2^l) \cos \phi \quad (17)$$

The third constraint \mathcal{C}_3 defines the relative rotation angle ϕ . These constraints are enforced via a Lagrange multiplier technique. The forces of constraint associated with these constraints are:

$$\begin{aligned} \underline{f}^k &= s\lambda_1 \tilde{e}_3^k e_1^l + s\lambda_2 \tilde{e}_3^k e_2^l + s\lambda_3 \tilde{e}_1^k (\sin \phi e_1^l + \cos \phi e_2^l) \\ \underline{f}^l &= -s\lambda_1 \tilde{e}_3^k e_1^l - s\lambda_2 \tilde{e}_3^k e_2^l - s\lambda_3 \tilde{e}_1^k (\sin \phi e_1^l + \cos \phi e_2^l) \\ f^\phi &= s\lambda_3 e_1^{kT} (\cos \phi e_1^l - \sin \phi e_2^l) \end{aligned} \quad (18)$$

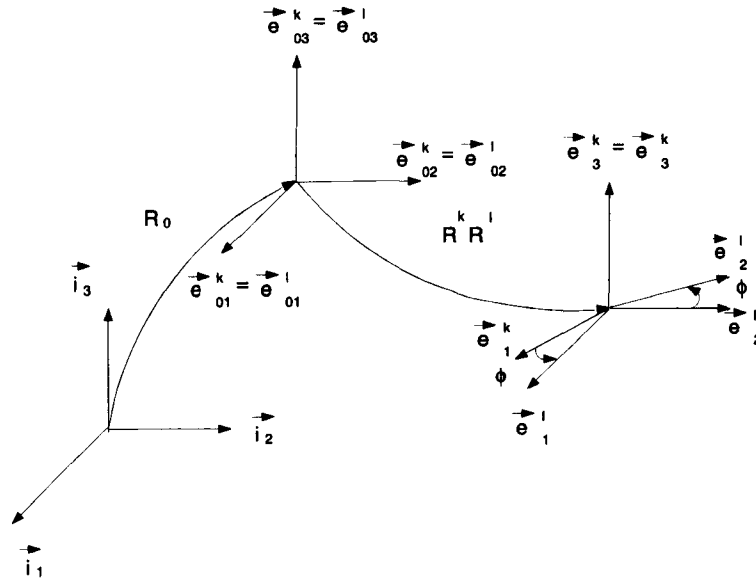


Figure 2. Kinematics of a revolute joint

where f^k and f^l are the constraint moments applied on body k and l , respectively, and f^ϕ the constraint force associated with the degree of freedom ϕ ; λ_1 , λ_2 and λ_3 the Lagrange multipliers used to enforce the constraint \mathcal{C}_1 , \mathcal{C}_2 and \mathcal{C}_3 , respectively, and s a scaling factor.

The forces of constraint associated with \mathcal{C}_1 are discretized as

$$f_1^k = s\lambda_1 \left(\frac{2R_{n+1/2}^k R_0}{4 - a_0^k} i_3 \right) \frac{R_{n+1}^l R_0 + R_n^l R_0}{2} i_1 \tag{19}$$

$$f_1^l = s\lambda_1 \left(\frac{2R_{n+1/2}^l R_0}{4 - a_0^l} i_1 \right) \frac{R_{n+1}^k R_0 + R_n^k R_0}{2} i_3$$

Similar expressions hold for the forces of constraint f_2^k and f_2^l corresponding to constraint \mathcal{C}_2 , and the forces of constraint corresponding to constraint \mathcal{C}_3 are discretized as:

$$f_3^k = s\lambda_3 \left(\frac{2R_{n+1/2}^k R_0}{4 - a_0^k} i_1 \right) \frac{R_{n+1}^l R_0 + R_n^l R_0}{2} v_\phi$$

$$f_3^l = s\lambda_3 \left(\frac{2R_{n+1/2}^l R_0}{4 - a_0^l} v_\phi \right) \frac{R_{n+1}^k R_0 + R_n^k R_0}{2} i_1 \tag{20}$$

$$f_3^\phi = s\lambda_3 \left(\frac{e_{1n+1}^{iT} e_{1n+1}^k + e_{1n}^{iT} e_{1n}^k}{2} \cos \phi_{n+1/2} - \frac{e_{2n+1}^{iT} e_{1n+1}^k + e_{2n}^{iT} e_{1n}^k}{2} \sin \phi_{n+1/2} \right)$$

It is well known that the forces of constraint perform no work during the dynamic response of the system. We now wish to find under which condition the work done by the *discretized* forces also vanishes. To that effect the work done by the discretized forces of constraint ΔW_{const} during a time step is computed. Using relationships (49) and (55) we find

$$\frac{\Delta W_{\text{const}}}{\Delta t} = s\lambda^T \frac{\mathcal{C}_{n+1} - \mathcal{C}_n}{\Delta t}$$

Clearly the work done by the discretized forces of constraint vanishes if

$$\frac{\mathcal{C}_{n+1} - \mathcal{C}_n}{\Delta t} = 0 \quad (21)$$

This clearly corresponds to a weak enforcement of the constraint (16), written as $\mathcal{C}_{n+1/2} = 0$. To avoid the drift phenomenon associated with the enforcement of equation (21) it is preferable to enforce

$$\mathcal{C}_{n+1} = 0 \quad (22)$$

Enforcing this constraint at each step implies equation (21) which in turn implies the vanishing of the work done by the discretized forces of constraint associated with the revolute joint.

The discretization of the beam equations of motion (12) and (14), together with the discretization of the forces of constraint (19) and (20) and constraint (22) provides an unconditionally stable integration procedure for non-linear multi-body problems.

A variety of kinematic constraints can be developed as outlined above, so that general multi-body configurations can be modelled effectively.

4. NUMERICAL EXAMPLES

In this section, three numerical examples are presented to assess the advantages and drawbacks of the fore mentioned energy preserving integration scheme. The first example deals with a 2.4 m long uniform straight beam, hinged at the root as to allow rotation about the \tilde{e}_2 axis and free at the tip. The beam is initially at rest, with \mathcal{S}_0 aligned with \mathcal{S} everywhere and subjected to a linearly varying ramp load at its tip. This load starts at zero at time $t = 0$ and reaches its maximum value at $t = 0.025$ s, with components of 1000 N in both \tilde{i}_2 and \tilde{i}_3 directions. The physical properties of the beam are summarized in Table I.

Table I. Convergence study: beam properties

| <i>Sectional Stiffness Properties</i> | |
|--|--------------------------------|
| Axial stiffness: | 4.35080E + 07 N |
| Shear stiffness in \tilde{e}_2 direction: | 1.40385E + 07 N |
| Shear stiffness in \tilde{e}_3 direction: | 2.80769E + 06 N |
| Torsional stiffness: | 2.80514E + 04 N m ² |
| Bending stiffness, about \tilde{e}_2 : | 2.32577E + 04 N m ² |
| Bending stiffness, about \tilde{e}_3 : | 2.98731E + 05 N m ² |
| <i>Sectional Mass Properties</i> | |
| Mass | 1.60920E + 00 kg/m |
| Mass moment of inertia about \tilde{e}_1 : | 1.19092E - 02 kg m |
| Mass moment of inertia about \tilde{e}_2 : | 8.60200E - 04 kg m |
| Mass moment of inertia about \tilde{e}_3 : | 1.10490E - 02 kg m |

The beam is modelled with four cubic beam elements and the hinge with a revolute joint element. The dynamic response of the beam was calculated with the generalized- α method,¹¹ with $\rho_\infty = 0.5$ (ρ_∞ is the spectral radius at infinite frequency), and the energy preserving scheme. The analysis was first performed with 250 equal time steps and then repeated with 500, 1000, 2000 and 4000 steps. In general, the results of the two methods were found to be in good agreement. Some of the time histories calculated with the energy preserving scheme contained higher levels of high frequency oscillation than the corresponding results from the generalized- α method, but this is to be expected considering the absence of numerical dissipation in the energy preserving scheme. Since no analytical solution exist for this problem, the solution computed with 4000 time steps, was considered a 'reference' solution. The normalized error in tip displacements, velocities, and root moments, with respect to the reference solution, are plotted in Figure 3 as functions of the number of time steps. This convergence study confirms the second order accuracy of both methods.

The second example deals with the flexible elbow mechanism depicted in Figure 4. It consists of two straight 0.72 m long aluminum beams of rectangular cross section (5 mm \times 1 mm), the first of which is initially along \hat{i}_1 and supported at its root by a hinge as to allow rotation about the \hat{i}_3 axis. The second beam hinges at its root on the tip of the first beam with a revolute joint of which the axis is aligned with beam 1. Two masses of 500 g each are rigidly connected at the tip of each of the two beams. The beam cross sections are oriented in such a way that the smaller of the two bending stiffnesses is about the \hat{e}_3 axis, in both cases. The modulus of elasticity, Poisson constant and density of aluminum are 73 GN/m², 0.3 and 2700 kg/m³ respectively.

The system is initially at rest. The loading of the system consist of a triangular pulse load applied to the tip of beam 1, acting in the \hat{i}_2 direction, and a triangular pulse torque between the two beams. The direction of the torque is such as to accelerate beam 2 about the negative of its

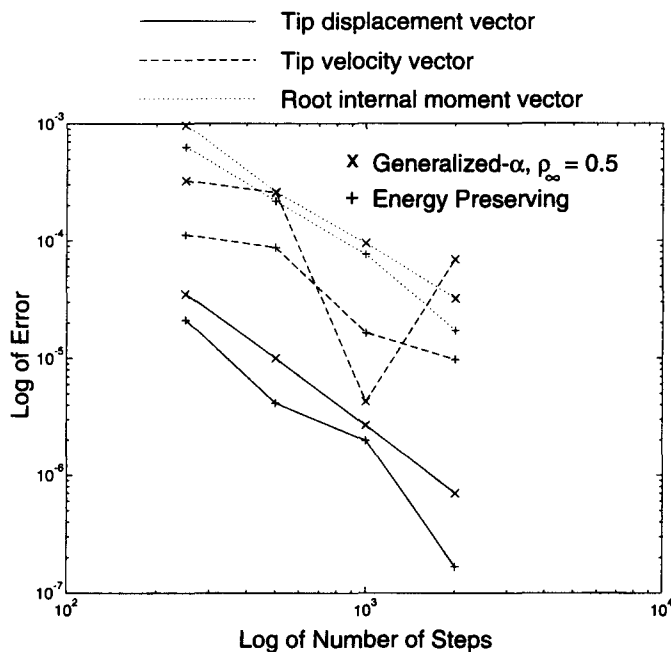


Figure 3. Error in tip displacement and velocity, and root internal moment vectors

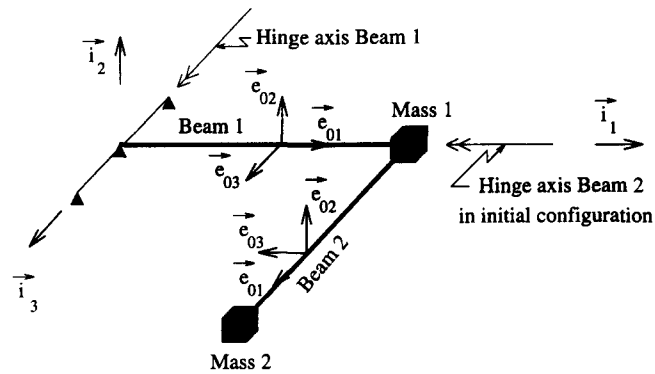


Figure 4. Flexible elbow mechanism, in the initial configuration

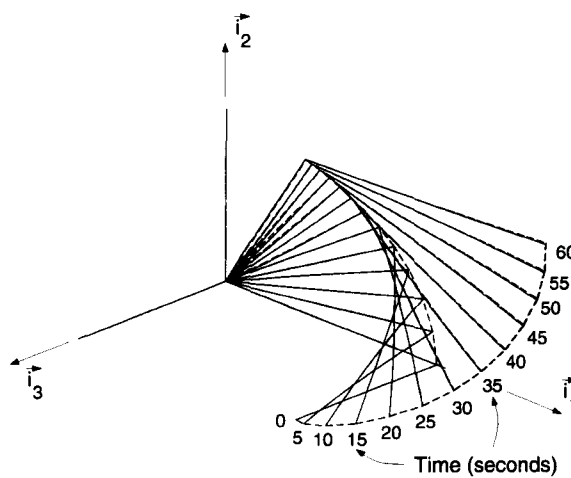


Figure 5. Flexible elbow mechanism: motion and deformation of beams

root \hat{e}_3 axis. The duration of both pulses is 0.256 seconds, peaking at 0.128 seconds with a 0.1 N value for the tip load and a 0.01 Nm value for the torque.

The system was modelled with 12 cubic beam elements for each beam, two revolute joint elements and two rigid masses, for a total of 446 degrees of freedom. The dynamic response of the system was computed with the generalized- α method ($\rho_\infty = 0.5$), and the energy preserving scheme, for a period of 100 s, using a total of 25 000 equal time steps. The energy preserving scheme failed to converge at the 15 620th time step, at 62.48 s, most probably due to significant high frequency content of the predicted response. Up to this point, however, the two methods are in fairly good agreement. It should be noted that the trapezoidal rule ($\rho_\infty = 1$), which does not provide numerical dissipation, is unstable for this problem.

The motion and deformation of the two beams are shown in Figure 5. In this figure, the position of the two beams at 5 s intervals are plotted on a three dimensional graph: the solid lines corresponding to the results of the energy preserving scheme and the dashed lines corresponding to those of the generalized- α method. The results of the two methods are in very good agreement.

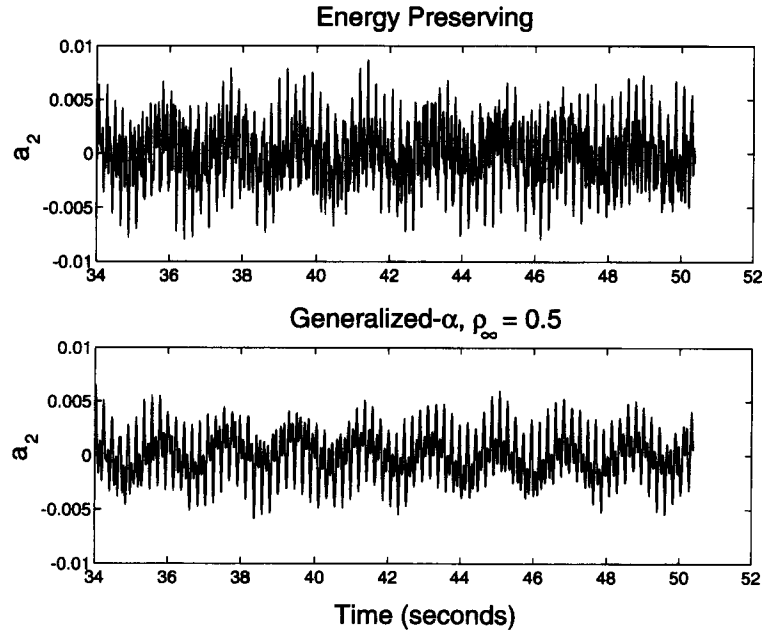


Figure 6. Flexible elbow mechanism: time history of conformal rotation vector component a_2 at mass 1 measured in the triad associated with the root of beam 1

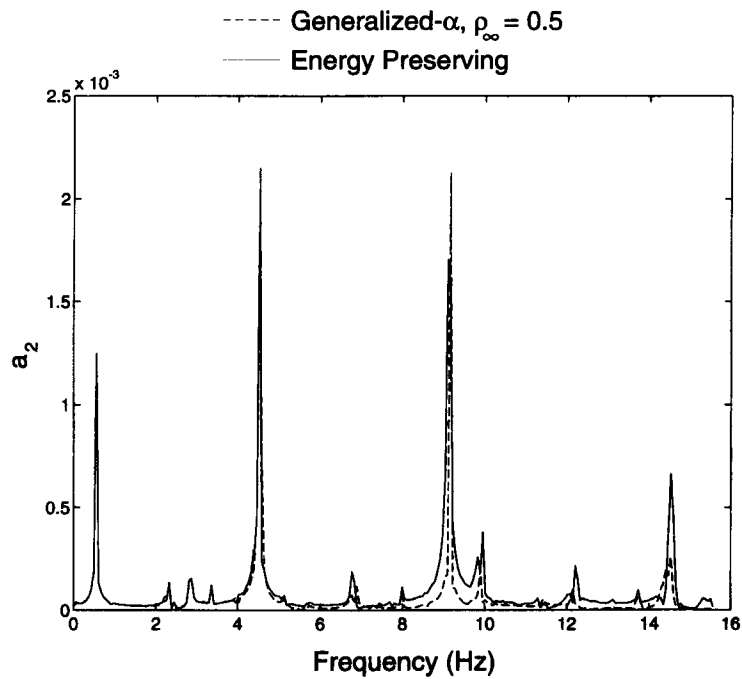


Figure 7. Flexible elbow mechanism: spectrum of conformal rotation vector component a_2 at mass 1 measured in the triad associated with the root of beam 1

In addition to the large overall motion depicted in Figure 5, a number of vibratory modes are also excited. By far the most significant of these is the torsional response of beam 1; a Fourier analysis (with a 0.178 Hz resolution) revealed a single frequency response at 2.310 and 2.308 Hz in the case of the energy preserving scheme and generalized- α method, respectively, both cases with an amplitude of 14.9° , at mass 1. These results are in good agreement with those predicted by an eigenvalue analysis of the system in the reference configuration, which yields a torsional natural frequency of beam 1 of 2.309 Hz. Beam 2 does not participate in this mode.

Some other vibration results are presented as a group of paired graphs, Figures 6–11. The second graph of each pair shows the frequency content of the responses, obtained by Fourier analysis of the time history shown in the first graph of each pair. Each frequency graph is scaled in such a way that the vertical axis may directly be interpreted as an amplitude axis. No windowing was used during the Fourier analyses, which may lead to inaccuracies in amplitude values due to smearing. It is also important to note that for the time step $\Delta t = 4 \times 10^{-3}$ s used in the analysis, a frequency of 2.5 Hz corresponds to 100 time steps per period ($\Delta t/T = 0.01$) whereas 25 Hz corresponds to $\Delta t/T = 0.1$. At this latter frequency, the generalized- α method ($\rho_\infty = 0.5$) already involves a significant amount of numerical dissipation.

The first pair of graphs, Figures 6 and 7, show the results pertaining to the conformal rotation vector component a_2 at mass 1, measured in the triad associated with the root of beam 1. These are indicative of bending vibrations of beam 1, about the \hat{i}_2 axis. The spectra were obtained with 4096 point fast Fourier transforms (FFTs). Even though the time histories of a_2 calculated with the two methods are quite different, the difference seems to be primarily due to the presence of high frequency oscillations in the energy preserving scheme. Indeed, Figure 7 shows that the results of the two methods are in good agreement as far as low frequencies are concerned (peaks at 0.55, 4.52 and 9.16 Hz). The effect of numerical dissipation of the generalized- α method is apparent for the peak at 14.52 Hz. At this frequency the system would have completed 489 oscillations between the termination of the applied load pulse and the start of the FFT time history at $t = 34$ s.

The next pair of graphs, Figures 8 and 9, shows the results pertaining to the transverse shear force in the \hat{e}_3 direction, at the Gauss point closest to the root of beam 1. Once again, the energy preserving scheme results show a very significant high frequency content. The spectra, both obtained with 4096 point FFTs, show good agreement with respect to the lowest peak at 0.55 Hz: both methods report amplitudes of 3.46×10^{-3} N. Both agree on the placement of peaks at other frequencies and on their amplitudes, but at 14.52 Hz the generalized- α method has already damped out the oscillation significantly. Note that the smearing associated with the FFT is also contributing to discrepancies between the results of the two methods. FFT results for the energy preserving scheme reveal high amplitude oscillations at various frequencies around 20 Hz, which are probably responsible for the superposed 'noise' evident in the time history.

The last pair of graphs deals with the behavior of beam 2, and depicts the transverse displacement of mass 2 in the \hat{e}_2 direction, relative to the root of beam 2, and measured in the triad attached at this root. With respect to the dominant frequency, the results of the two methods in the time histories, shown in Figure 10, are in good agreement. The spectra, shown in Figure 11, were both obtained with 1412 point discrete Fourier transforms, implying a frequency resolution of 0.18 Hz. Both peak at 2.83 Hz with an amplitude of 29.8 mm, which confirms the good agreement of the dominant frequency. The eigenvalue analysis of the system in its initial configuration indicated that the fifth elastic mode is at 2.90 Hz. This mode involves primarily a bending vibration of beam 2, about its \hat{e}_3 axis, with virtually no participation of beam 1, and is not expected to change with large rotations of the system components. It is evident from these results that vibration in this mode was also significantly excited by the applied pulse loading.

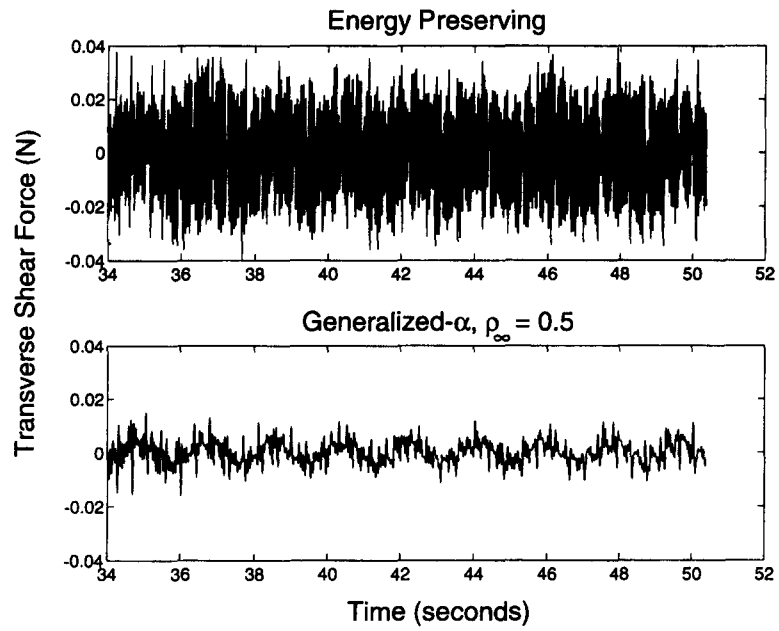


Figure 8. Flexible elbow mechanism: time history of transverse shear force in \hat{e}_3 direction at root of beam 1

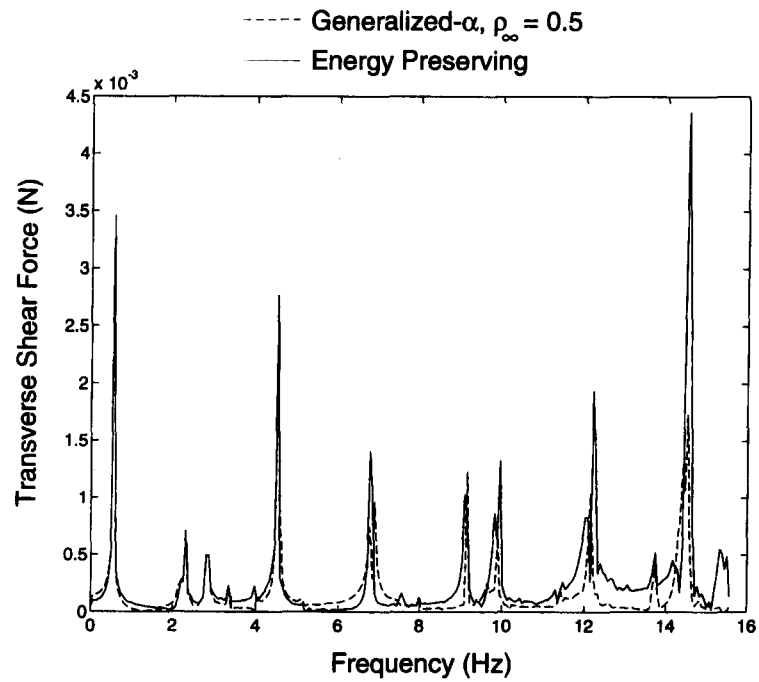


Figure 9. Flexible elbow mechanism: spectrum of transverse shear force in \hat{e}_3 direction at root of beam 1

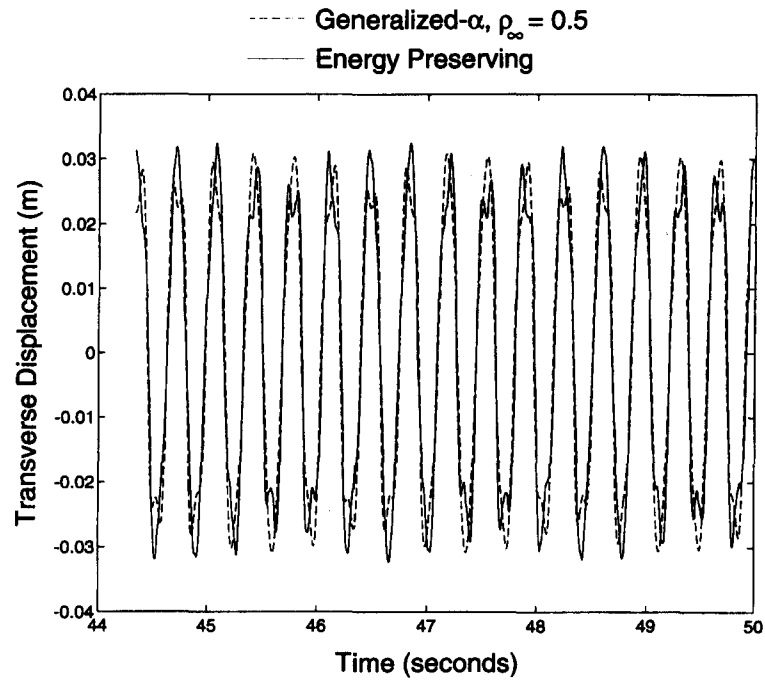


Figure 10. Flexible elbow mechanism: time history of transverse displacement of mass 2 in the \bar{e}_2 direction relative to, and measured in the triad associated with the root of beam 2

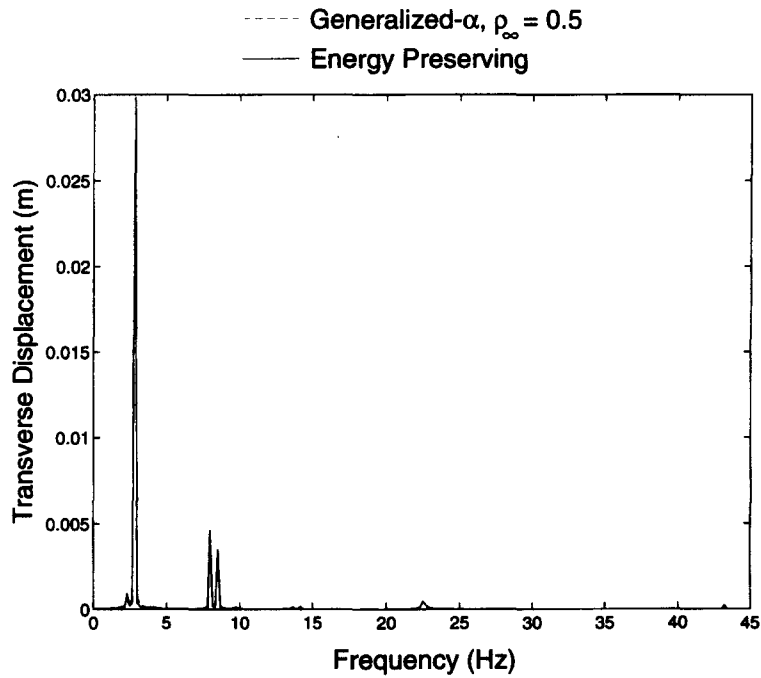


Figure 11. Flexible elbow mechanism: spectrum of transverse displacement of mass 2 in the \bar{e}_2 direction relative to, and measured in the triad associated with the root of beam 2

Even though the two amplitude values of the second peak in the spectra (at 7.97 Hz) are in reasonable agreement, the two methods predict responses with a 138° phase difference. This phase difference is evident in the time histories depicted in Figure 10.

The third numerical example deals with the swing, shown in Figure 12, which consists of a beam and a mid-span mass, with physical properties identical to those of either beams or masses of the flexible elbow mechanism. Everywhere along the span of the beam \mathcal{S}_0 is aligned with \mathcal{S} , and the beam cross section is oriented in such a way that the smaller of the two bending stiffnesses is about the \bar{e}_2 axis. The mass is rigidly connected to the beam at its mid-span position, labelled C in the figure. The beam is suspended at each end by two rigid links, and is initially at rest in the position as shown in the Figure 12. The rigid links impose a kinematic constraint corresponding to fixed distance between points O_1 and A, and O_2 and E of 0.36 and $0.36\sqrt{2}$ m, respectively. The points labelled B and D indicate the quarter and three quarter span points of the beam, respectively. The loading of the system consist of a triangular pulse in the \bar{i}_1 direction applied at the mid-span mass. This pulse starts at time $t = 0$, peaks at 2 N at $t = 0.128$ s and terminates at $t = 0.256$ s.

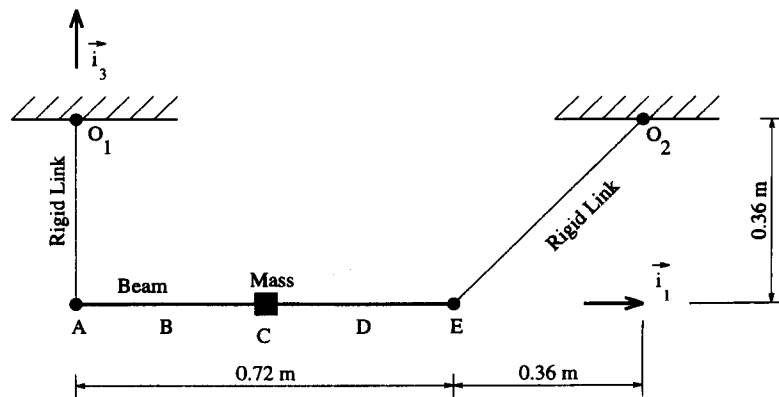


Figure 12. Swing comprising two rigid links and a beam with midspan mass

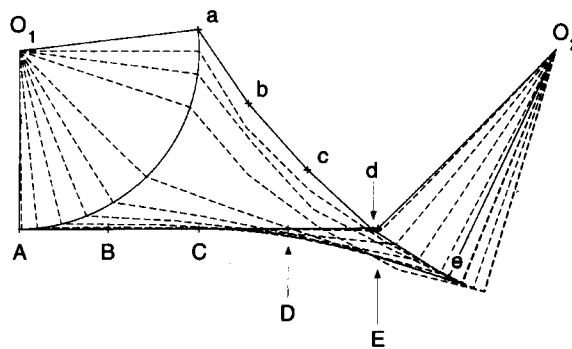


Figure 13. Swing: motion and deformation of beam and motion of links, at 0.1 s intervals, with solid lines indicating positions at $t = 0$ and 1 s, and the locus of point A

The system was modelled with four equal length cubic beam elements, two rigid links and a rigid mass, for a total of 80 degrees of freedom. The dynamic response of the system was calculated over a 1 s period using both the energy preserving scheme and the generalized- α method, ($\rho_\infty = 0.5$), in each case with 2000 equal time steps of $\Delta t = 0.5 \times 10^{-3}$ s.

Figure 13 shows the overall response of the system: the deflected beam configuration predicted by the energy preserving scheme is shown at 0.1 s intervals. The solid lines indicate the initial and final configurations, as well as the circular arc locus of point A. The significant elastic deformation of the beam is evident in this figure.

The loci of various points on the beam are depicted in Figure 14 where the initial and final configurations of the beam are shown in dashed lines. As expected, points A and E follow circular arcs, even though point E reverses its direction of motion some time during the 1 s period. At $t = 0.641$ s, link O_1 -A and the beam line up approximately (at this point the beam is no longer perfectly straight). This event (labelled 'event X') has considerable impact on the dynamic behaviour of the system. The motion of point C is quite smooth as a result of the high inertia attached at this point, except for an almost instantaneous change in direction at event X. This contrasts with the motions of points B and D which become highly vibratory after event X.

Figure 15 shows a comparison of the predicted time histories for the \vec{i}_1 and \vec{i}_3 direction displacement components of point B, for the energy preserving scheme and the generalized- α method. The two methods are in excellent agreement, small differences being barely visible only after event X.

Figure 16 shows the calculated time histories of the axial force at the Gauss point immediately to the left of the mid-span mass. The two methods are in close agreement until right after the high peak caused by event X. The peak value is predicted to be 115.8 and 112.7 N, for the energy preserving and generalized- α methods, respectively, and is predicted by both methods to occur at time $t = 0.641$ s. After this event the energy preserving scheme results show much more pronounced high frequency oscillations than the generalized- α method. Similar trends are observed when other variables are plotted: the displacement results of the two methods are in excellent agreement, while the velocities and internal forces are in excellent agreement up to event X, after which high levels of high frequency oscillation is observed in the energy preserving scheme results.

The convergence criterion used to predict the above responses is based on an energy-like quantity, and is written as

$$e_1 = \frac{\sqrt{|\Delta u^{kT} K \Delta u^k|}}{\sqrt{|\Delta u^{1T} K \Delta u^1|}} < \varepsilon \quad (23)$$

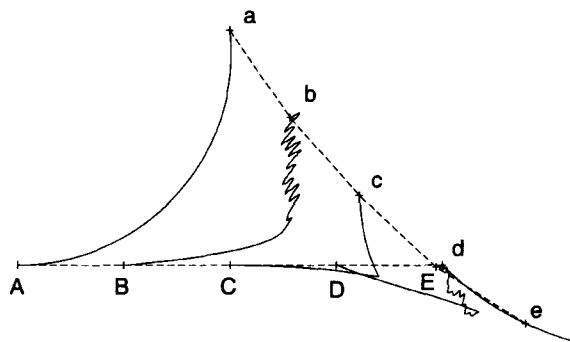


Figure 14. Swing: loci of five nodes on the beam

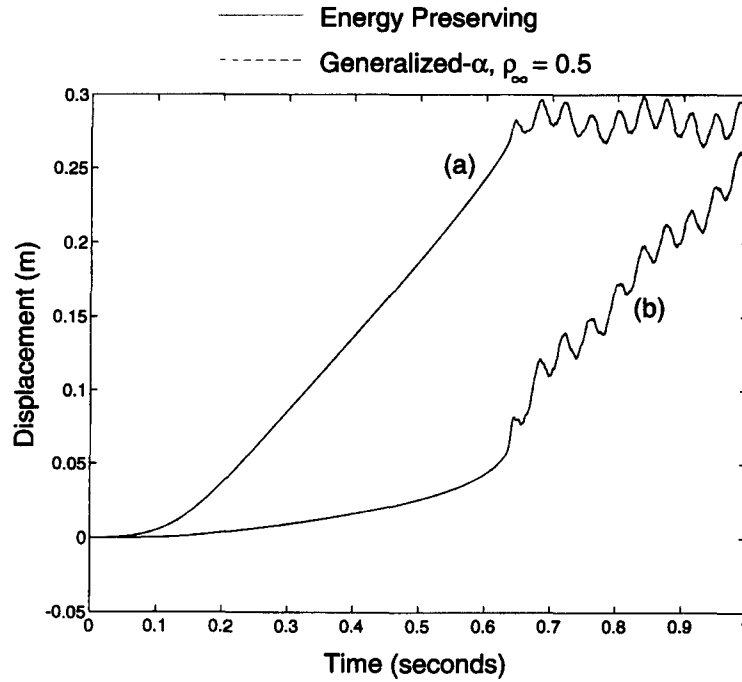


Figure 15. Swing: time history of displacement components of point B in the (a) \hat{i}_1 and (b) \hat{i}_3 directions

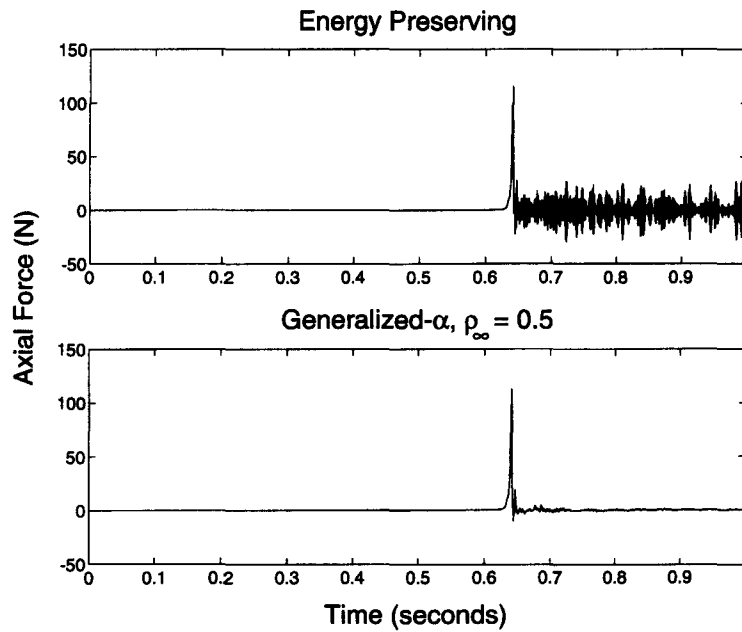


Figure 16. Swing: time history of axial force in the beam, at the Gauss point immediately to the left of the midspan mass

where K is the dynamic stiffness matrix, Δu^{kT} the displacement increment at the k -th iteration, and ε a small positive number. Let e_2 be the true energy norm defined by

$$e_2 = \left| \frac{E(t) - E(t_a)}{E(t_a)} \right| \quad (24)$$

where t_a is some reference time after the applied loads have been released.

If the non-linear equations of motion are solved exactly $e_1 = 0$, and this was shown in Sections 2 and 3 to imply $e_2 = 0$. In the practical implementation, iteration is stopped when $e_1 < \varepsilon$, and one would expect e_2 to become a small quantity as well. To verify this claim, both norms were computed and plotted in Figure 17. The convergence criterion is chosen as $e_1 < 10^{-6}$. Up to event X , $e_1 < 10^{-6}$ clearly implies e_2 to remain small. At event X , however, a jump of 6 orders of magnitude appears in e_2 . In other words satisfaction of the energy-like criterion $e_1 < \varepsilon$ does not necessarily imply strict energy preservation of the system.

In view of this problem, it seems natural to use the true energy of the system as a convergence criterion, i.e. $e_2 < \varepsilon$. The code was modified to use this new criterion. However the computation failed to converge under this new convergence criterion at $t = 0.6355$ s, i.e. during the early stages of event X . The time step was reduced by a factor of 10; this allowed the solution to proceed up to time $t = 0.6360$ s. Further reducing the time step by another order of magnitude resulted in convergence failure at time $t = 0.6301$ s. The history of the true energy norm with the various time steps is shown in Figure 18. This behaviour can probably be explained as follows. The energy like criterion (23) only involves increments in displacement, whereas the true energy criterion (24) depends on both displacements and velocities. During event X , large changes in velocity are present, rendering the convergence of the true energy norm more difficult. Selecting a smaller time step does not alleviate this problem because the smaller time step allows the resolution of increasingly higher frequency oscillations.

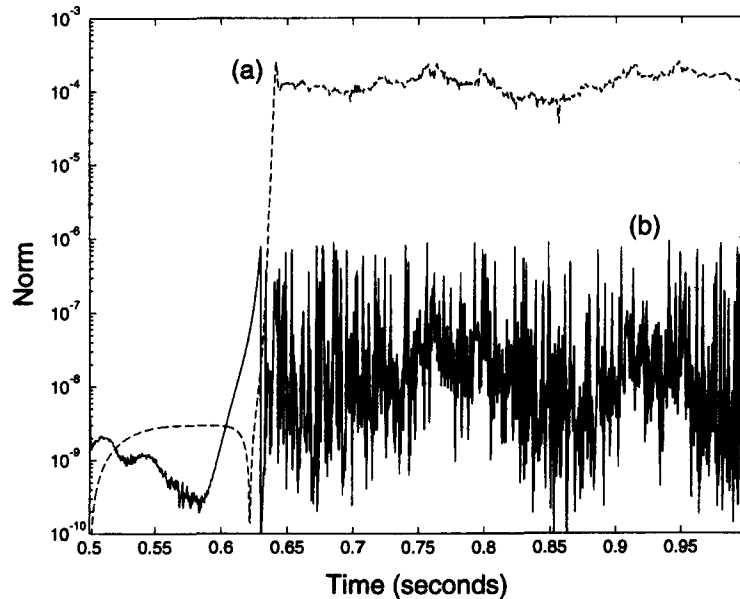


Figure 17. Swing: time history of (a) e_2 and (b) the energy-like norm e_1

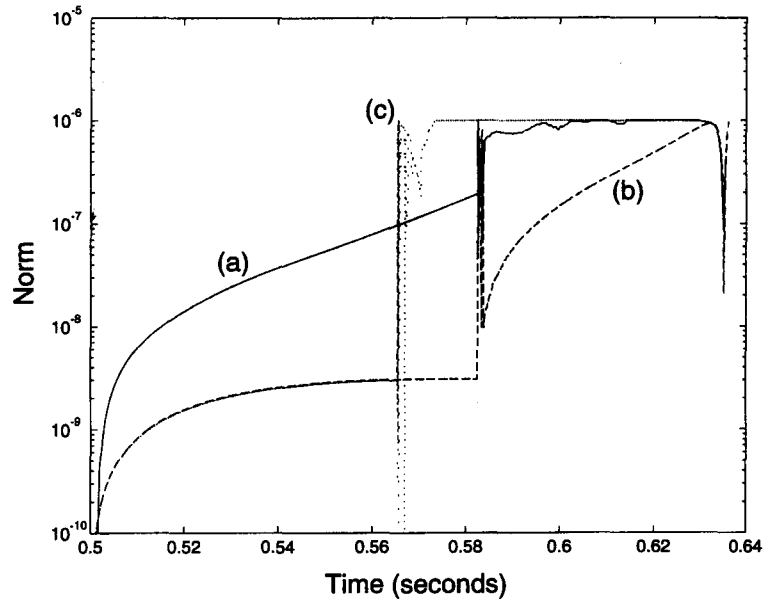


Figure 18. Swing: time history of e_2 for (a) $\Delta t = 5.0 \times 10^{-4}$, (b) $\Delta t = 5.0 \times 10^{-5}$, (c) $\Delta t = 5.0 \times 10^{-6}$ s

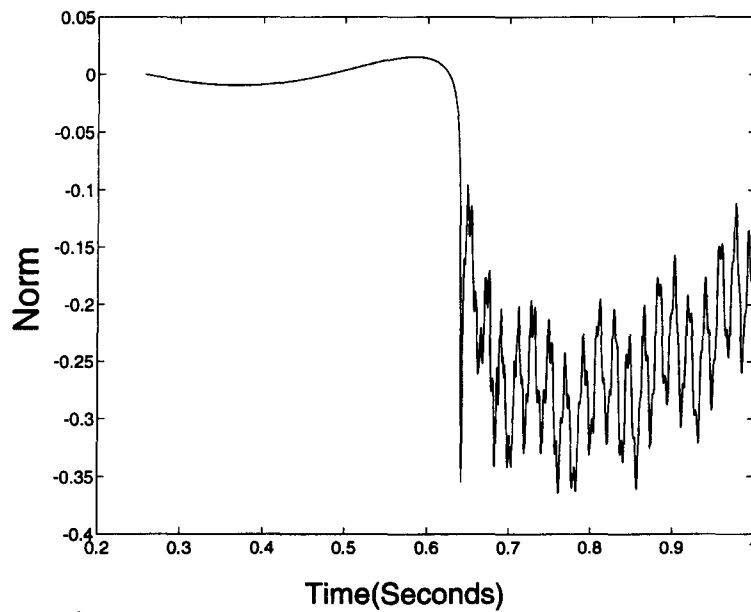


Figure 19. Swing: Time history of the true energy norm for the generalized- α method

The above discussion shows that when the dynamic response of the system is smooth, the use of either the energy or the energy-like norm is equivalent. However, in the presence of high frequencies, the satisfaction of the energy-like norm does not necessarily imply strict energy preservation. Furthermore, numerical experimentation showed that satisfaction of the true energy norm criterion does not imply the satisfaction of the energy-like criterion.

It should be noted that the generalized- α method has no convergence problems with a time step $\Delta t = 0.5 \times 10^{-3}$ s (the energy-like norm criterion (23) was used), though energy preservation is clearly not implied by this convergence. Figure 19 shows the evolution of the true energy norm (24) for the generalized- α solution. The general trend is a decrease in the total energy of the system, as expected from the dissipation characteristics of this method. At event X, 30 per cent of the total energy of the system is numerically dissipated in eight time steps only. However, 25 per cent of the total energy is numerically created in the next six time steps. This clearly shows the shortcomings of using a method which stability has only been established for linear systems. For linear systems, the generalized- α method only dissipated energy, thus establishing the unconditional stability of the scheme. However, when applied to a non-linear system, energy can be created in the numerical solution process, and hence, lead to potential instabilities.

5. DISCUSSION AND CONCLUSIONS

The equations of motion resulting from the modelling of multi-body systems with the finite element method are stiff, non-linear, differential-algebraic equations. Time integration of these equations is a difficult task as instabilities and high frequency numerical oscillations are often present.

The classical trapezoidal rule, which is proved to be unconditionally stable for linear systems, was shown to be weakly unstable in the presence of kinematic constraints by Cardona and Geradin.⁵ The same authors used the HHT scheme to overcome this weak instability. This approach, however, cannot be proved to be stable for non-linear systems. In fact, the last example presented in this paper shows that, in a specific case, a large increase in the total energy of the system is possible. This is clearly incompatible with an unconditionally stable method.

In this paper an alternate approach was followed. Discretized equations for the dynamic response of elastic beams were presented that imply preservation of the total energy. Discretized constraint forces corresponding to the kinematic constraints associated with a revolute joint were derived and shown to perform no work during the evolution of the system. The combination of the above features of the model guarantees unconditional stability of the overall integration process for non-linear multi-body systems as it implies preservation of the total energy of the system.³ Numerical experimentation shows that the strict energy preservation implied by the exact solution of the discretized equations of motion is indeed satisfied to a high level of precision. The formal proof of stability derived in this paper for non-linear elastic multi-body systems represents a significant improvement over existing methodologies for which stability is only proved for linear systems. The accuracy and cost of the proposed scheme are similar to those of the HHT or generalized- α schemes.

High frequency oscillations were observed in the response predicted by the energy preserving scheme. The presence of these high frequency oscillations is due to the complex nature of the dynamic response of multi-body systems and the lack of high frequency numerical dissipation of the energy preserving scheme. The absence of high frequency numerical dissipation can result in undesirable response features. First, the time history of internal forces and velocities can present a very significant high frequency content. Second, it seems that in some pathological cases involving significant high frequency content due to shocks such as presented in the third example, the presence of high frequency oscillations can hinder the convergence process for the solution of the non-linear equations of motion. The selection of a smaller time step does not necessarily help this convergence process, as a smaller time step allows even higher frequency oscillations to be present in the response. The development of 'energy decaying' schemes, i.e. schemes eliminating

the energy associated with vibratory motions at high frequency, will be presented in a subsequent paper.

ACKNOWLEDGMENTS

This research was sponsored by the US Army Research Office, under Grant Number DAAH04-93-G-0003; Dr. Robert E. Singleton is the contract monitor.

APPENDIX I. THE CONFORMAL ROTATION VECTOR.

Let e_0 and \underline{e} be the Euler parameters representing a finite rotation.¹⁰ Consider now the following conformal transformation which defines c_0 and the components of the conformal rotation vector \underline{c} :

$$c_0 = \frac{4e_0}{1+e_0}, \quad \underline{c} = \frac{4\underline{e}}{1+e_0}, \quad e_0 = \frac{c_0}{4-c_0}, \quad \underline{e} = \frac{\underline{c}}{4-c_0} \quad (25)$$

where the dependent parameter $c_0 = 2 - (c_1^2 + c_2^2 + c_3^2)/8$.

The geometric interpretation of the conformal rotation vector is easily derived from its definition as

$$\underline{c} = 4\underline{u} \tan \frac{\phi}{4} \quad (26)$$

where ϕ is the magnitude of the finite rotation and \underline{u} the components of the unit vector about which it takes place. The following matrix is defined:

$$G(\underline{c}) = \frac{1}{4-c_0} \left(c_0 I + \tilde{c} + \frac{\underline{c} \cdot \underline{c}^T}{4} \right) \quad (27)$$

It enjoys the following remarkable properties:

$$GG^T = I, \quad G\underline{c} = \underline{c} \quad (28)$$

$$G + \frac{\tilde{c}^T}{4-c_0} = G^T - \frac{\tilde{c}^T}{4-c_0} = \left(\frac{G + G^T}{2} \right) \quad (29)$$

$$\left(I + \frac{\tilde{c}^T}{c_0} \right) G = \left(I - \frac{\tilde{c}^T}{c_0} \right) G^T = \left(\frac{G + G^T}{2} \right)^{-1} \quad (30)$$

$$\frac{2\tilde{c}}{4-c_0} = G - G^T \quad (31)$$

The rotation matrix defined by \underline{c} can be easily written as

$$R(\underline{c}) = \frac{1}{(4-c_0)} (c_0^2 I + 2c_0 \tilde{c} + \tilde{c}\tilde{c} + \underline{c} \cdot \underline{c}^T) = G(\underline{c})G(\underline{c}) \quad (32)$$

This last relationship shows that the conformal rotation vector can be conveniently used to express the half rotation (through $G(\underline{c})$), and the rotation (through $R(\underline{c})$). All these expressions are purely algebraic.

APPENDIX II. DISCRETIZATION OF THE FINITE ROTATIONS

Consider an initial time t_i , a final time t_f and a mid-point time $t_h = (t_i + t_f)/2$ and the corresponding triads \mathcal{S}_i , \mathcal{S}_f and \mathcal{S}_h , respectively. The rotation matrices associated with those triads are R_i , R_f , and R_h respectively, all measured in \mathcal{S} . $R(\underline{c})$ is the rotation matrix from \mathcal{S}_i to \mathcal{S}_f , measured in \mathcal{S} . The mid-point triad \mathcal{S}_h is defined so that the rotation from \mathcal{S}_i to \mathcal{S}_h and \mathcal{S}_h to \mathcal{S}_f are equal. Let G be that rotation, measured in \mathcal{S} . Let G^* and R^* be the corresponding rotation matrices measured in \mathcal{S}_h . The following relationship are readily derived:

$$\begin{aligned} G &= R_h R_i^T, & G^* &= R_0^T R_i^T R_h R_0 \\ G &= R_f R_h^T, & G^* &= R_0^T R_h^T R_f R_0 \\ R &= R_f R_i^T, & R^* &= R_0^T R_h^T R_f R_0 R_0^T R_i^T R_h R_0 \end{aligned} \quad (33)$$

and

$$\begin{aligned} R_f R_0 &= R_h R_0 G^* = R_i R_0 R^* \\ R_h R_0 &= R_i R_0 G^* = R_f R_0 G^{*T} \\ R_i R_0 &= R_h R_0 G^{*T} = R_f R_0 R^{*T} \end{aligned} \quad (34)$$

Finally, the following notations are induced:

$$\mathcal{R}_i = \begin{bmatrix} R_i R_0 & 0 \\ 0 & R_i R_0 \end{bmatrix}, \quad \mathcal{R}_f = \begin{bmatrix} R_f R_0 & 0 \\ 0 & R_f R_0 \end{bmatrix} \quad (35)$$

APPENDIX III. DISCRETIZATION OF THE EQUATIONS OF MOTION OF A BEAM

Consider the following discretization of the beam equations of motion (11):

$$\begin{aligned} \frac{\mathcal{R}_f p_f^* - \mathcal{R}_i p_i^*}{\Delta t} + \mathcal{U} \left[\frac{\tilde{u}_f - \tilde{u}_i}{\Delta t} \frac{2R_h R_0}{4 - c_0} \right] \frac{p_i^* + p_f^*}{2} \\ - (\mathcal{Q}_h g_h^*)' - \mathcal{U} \left[\frac{2}{c_0} (\tilde{u}'_0 + \tilde{u}'_h) \right] \mathcal{Q}_h g_h^* = \underline{q}_h \end{aligned} \quad (36)$$

where

$$\mathcal{Q}_h = \begin{bmatrix} \frac{R_f R_0 + R_i R_0}{2} & 0 \\ 0 & \frac{2R_h R_0}{4 - c_0} \end{bmatrix}$$

the mid-point displacement is defined as $\underline{u}_h = (\underline{u}_i + \underline{u}_f)/2$, and the elastic forces \underline{g}_h^* will be determined later.

Premultiplying these discretized equations by

$$\begin{bmatrix} \frac{\underline{u}_f^T - \underline{u}_i^T}{\Delta t} & \frac{\underline{c}^T}{\Delta t} \end{bmatrix}$$

and integrating over the span of the beam yields:

$$\int_0^L \left[\frac{\underline{u}_f^T - \underline{u}_i^T \underline{c}^T}{\Delta t} \right] \left[\frac{\mathcal{R}_f p_f^* - \mathcal{R}_i p_i^*}{\Delta t} + \mathcal{U} \left[\frac{\tilde{u}_f - \tilde{u}_i}{\Delta t} \frac{2R_h R_0}{4 - c_0} \right] \frac{p_i^* + p_f^*}{2} - (\mathcal{Q}_h g_h^*)' - \mathcal{U} \left[\frac{2}{c_0} (\tilde{u}'_0 + \tilde{u}'_h) \right] \mathcal{Q}_h g_h^* - q_h \right] dx_1 = 0$$

Integration by parts now yields

$$\int_0^L \left[\frac{\underline{u}_f^T - \underline{u}_i^T \underline{c}^T}{\Delta t} \right] \left[\frac{\mathcal{R}_f p_f^* - \mathcal{R}_i p_i^*}{\Delta t} + \mathcal{U} \left[\frac{\tilde{u}_f - \tilde{u}_i}{\Delta t} \frac{2R_h R_0}{4 - c_0} \right] \frac{p_i^* + p_f^*}{2} \right] dx_1 + \int_0^L \left\{ \left[\frac{\underline{u}_f^T - \underline{u}_i^T \underline{c}^T}{\Delta t} \right] - \left[\frac{\underline{u}_f^T - \underline{u}_i^T \underline{c}^T}{\Delta t} \right] \mathcal{U} \left[\frac{2}{c_0} (\tilde{u}'_0 + \tilde{u}'_h) \right] \right\} \mathcal{Q}_h g_h^* dx_1 = \frac{\Delta W}{\Delta t} \tag{37}$$

where ΔW is the work done by the externally applied forces during a time step.

Focusing on the inertial terms in the above equation and using relationships (34), the first integral becomes

$$\int_0^L \left[\frac{\underline{u}_f^T - \underline{u}_i^T}{\Delta t} R_h R_0 \underline{c}^{*T} \right] \left\{ \left[\begin{array}{cc} G^* + \frac{\tilde{c}^{*T}}{4 - c_0} & 0 \\ 0 & I \end{array} \right] \frac{p_f^*}{\Delta t} - \left[\begin{array}{cc} G^{*T} - \frac{\tilde{c}^{*T}}{4 - c_0} & 0 \\ 0 & I \end{array} \right] - \frac{p_i^*}{\Delta t} \right\} dx_1$$

Invoking first equation (29) and then once more relationship (34), this integral may be written as

$$\int_0^L \underline{v}_h^{*T} \frac{p_f^* - p_i^*}{\Delta t} dx_1 = \frac{1}{\Delta t} \int_0^L \underline{v}_h^{*T} M^* (\underline{v}_f^* - \underline{v}_i^*) dx_1 \tag{38}$$

where

$$\underline{v}_h^{*T} = \left[\frac{\underline{u}_f^T - \underline{u}_i^T}{\Delta t} \frac{R_f R_0 + R_i R_0}{2} \underline{c}^{*T} \right]$$

Focusing now on the elastic terms in equation (37), the second integral becomes

$$\frac{1}{\Delta t} \int_0^L \underline{g}_h^{*T} \left\{ \mathcal{Q}_h^T \left[\frac{\underline{u}'_f - \underline{u}'_i}{\underline{c}'} \right] - \mathcal{Q}_h^T \mathcal{U}^T \left[\frac{2}{c_0} (\tilde{u}'_0 + \tilde{u}'_h) \right] \right\} \left[\begin{array}{c} 0 \\ \underline{c} \end{array} \right] dx_1 \tag{39}$$

Using relationships (34), the first three components of the vector between the braces in equation (39) can be written as

$$\frac{G^{*T} + G^*}{2} R_0^T R_h^T \left[(\underline{u}'_0 + \underline{u}'_i) - (\underline{u}'_0 + \underline{u}'_i) + R_h R_0 \frac{\tilde{c}^{*T}}{c_0^*} R_0^T R_h^T (\underline{u}'_0 + \underline{u}'_i + \underline{u}'_0 + \underline{u}'_i) \right] = \frac{G^{*T} + G^*}{2} \left[\left(I + \frac{\tilde{c}^{*T}}{c_0^*} \right) R_0^T R_h^T (\underline{u}'_0 + \underline{u}'_i) - \left(I - \frac{\tilde{c}^{*T}}{c_0^*} \right) R_0^T R_h^T (\underline{u}'_0 + \underline{u}'_i) \right]$$

With the use of, once again, relationships (34), and equation (30), the above expression can be further simplified to

$$R_0^T R_f^T (\underline{u}'_0 + \underline{u}'_f) - R_0^T R_i^T (\underline{u}'_0 + \underline{u}'_i) = \underline{\epsilon}'_f - \underline{\epsilon}'_i \quad (40)$$

The last three components of the vector between the braces in equation (39) can be written as:

$$\frac{2R_0^T R_h^T}{4 - c_0^*} (R_h R_0 \underline{\epsilon}^*)'$$

With the help of relationships (34) it may be shown that

$$\frac{2R_0^T R_h^T}{4 - c_0^*} (R_h R_0 \underline{\epsilon}^*)' = \frac{2G^{*T}}{4 - c_0^*} [\underline{\epsilon}^{*'} + (\tilde{k}_0^* + \tilde{k}_i^*) \underline{\epsilon}^*] = \underline{k}'_f - \underline{k}'_i \quad (41)$$

Combining results (40) and (41), the elastic terms become

$$\frac{1}{\Delta t} \int_0^L \underline{g}_h^{*T} (\underline{\epsilon}'_f - \underline{\epsilon}'_i) dx_1 \quad (42)$$

Defining the elastic forces $\underline{g}_h^* = C^* \underline{\epsilon}_h^*$, where $\underline{\epsilon}_h^*$ are yet to be defined sectional strains, the expression (42) may be written as

$$\frac{1}{\Delta t} \int_0^L \underline{e}_h^{*T} C^* (\underline{e}'_f - \underline{e}'_i) dx_1 \quad (43)$$

Substituting the final expressions from (38) and (43) into equation (37) results in

$$\int_0^L \underline{v}_h^{*T} M^* (\underline{v}'_f - \underline{v}'_i) + \underline{e}_h^{*T} C^* (\underline{e}'_f - \underline{e}'_i) dx_1 = \Delta W \quad (44)$$

This fundamental scalar relationship is implied by the discretization (36) of the beam equations of motion.

APPENDIX IV. DISCRETIZATION OF THE FORCES OF CONSTRAINT IN A REVOLUTE JOINT

Consider the following discretization of the forces of constraint (17) corresponding to the constraint \mathcal{C}_1 :

$$\underline{f}_1^k = s\lambda_1 \left(\frac{2R_h^k \widetilde{R}_0}{4 - a_0^k} \underline{i}_3 \right) \frac{R_f^k R_0 + R_i^k R_0}{2} \underline{i}_1 \quad (45)$$

$$\underline{f}_1^l = s\lambda_1 \left(\frac{2R_h^l \widetilde{R}_0}{4 - a_0^l} \underline{i}_1 \right) \frac{R_f^l R_0 + R_i^l R_0}{2} \underline{i}_3 \quad (46)$$

The work done by these forces of constraint $\Delta W_{\text{const}}^{(1)}$ over a time step is

$$\frac{\Delta W_{\text{const}}^{(1)}}{\Delta t} = \frac{a^{kT}}{\Delta t} \underline{f}_1^k + \frac{a^{lT}}{\Delta t} \underline{f}_1^l \quad (47)$$

Introducing equations (45) and (46), and using equations (31) and (33) yields

$$\frac{\Delta W_{\text{const}}^{(1)}}{\Delta t} = \frac{s\lambda_1}{\Delta t} [i_1^T R_0^T R_h^{IT} (G^{IT} G^k - G^I G^{kT}) R_h^k R_0 i_3] \quad (48)$$

With the help of equation (33), this finally becomes

$$\frac{\Delta W_{\text{const}}^{(1)}}{\Delta t} = s\lambda_1 \frac{\mathcal{C}_{1f} - \mathcal{C}_{1i}}{\Delta t}. \quad (49)$$

Consider now the following discretization of the forces of constraint (17) corresponding to the constraint \mathcal{C}_3 :

$$f_3^k = s\lambda_3 \left(\frac{2R_h^k \widetilde{R}_0}{4 - a_0^k} i_1 \right) \frac{R_f^I R_0 + R_i^I R_0}{2} v_\phi \quad (50)$$

$$f_3^I = s\lambda_3 \left(\frac{2R_h^I \widetilde{R}_0}{4 - a_0^I} v_\phi \right) \frac{R_f^k R_0 + R_i^k R_0}{2} i_1 \quad (51)$$

$$f_3^\phi = s\lambda_3 \left(\frac{e_{1f}^{IT} e_{1f}^k + e_{1i}^{IT} e_{1i}^k}{2} \cos \phi_h - \frac{e_{2f}^{IT} e_{1f}^k + e_{2i}^{IT} e_{1i}^k}{2} \sin \phi_h \right) \quad (52)$$

where $\phi_h = (\phi_f + \phi_i)/2$, and

$$v_\phi = \frac{\sin \phi_f + \sin \phi_i}{2} i_1 + \frac{\cos \phi_f + \cos \phi_i}{2} i_2$$

The work done by these forces of constraint $\Delta W_{\text{const}}^{(3)}$ over a time step is

$$\frac{\Delta W_{\text{const}}^{(3)}}{\Delta t} = \frac{a^{kT}}{\Delta t} f_3^k + \frac{a^{IT}}{\Delta t} f_3^I + 2 \sin \frac{\phi_f - \phi_i}{2} f_3^\phi \quad (53)$$

Introducing equations (50)–(52), and using equations (31) and (33) yields

$$\begin{aligned} \frac{\Delta W_{\text{const}}^{(3)}}{\Delta t} = \frac{s\lambda_3}{\Delta t} \left[i_\phi^T R_0^T R_h^{IT} (G^{IT} G^k - G^I G^{kT}) R_h^k R_0 i_1 \right. \\ \left. + \frac{e_{1f}^{IT} e_{1f}^k + e_{1i}^{IT} e_{1i}^k}{2} (\sin \phi_f - \sin \phi_i) \right. \\ \left. - \frac{e_{2f}^{IT} e_{1f}^k + e_{2i}^{IT} e_{1i}^k}{2} (\cos \phi_i - \cos \phi_f) \right] \quad (54) \end{aligned}$$

With the help of equation (33), this finally becomes

$$\frac{\Delta W_{\text{const}}^{(3)}}{\Delta t} = s\lambda_3 \frac{\mathcal{C}_{3f} - \mathcal{C}_{3i}}{\Delta t} \quad (55)$$

REFERENCES

1. P. E. Nikravesh, *Computer-Aided Analysis of Mechanical Systems*. Prentice-Hall, Englewood Cliffs, N.J., 1988.
2. J. C. Simo and L. Vu-Quoc, 'A three dimensional finite strain rod model. Part II: computational aspects'. *Comput. Methods Appl. Mech. Eng.*, **58**, 79–116 (1986).

3. T. J. R. Hughes, *The Finite Element Method*, Prentice Hall, Englewood Cliffs, N.J., 1992.
4. N. M. Newmark, 'A method of computation for structural dynamics', *J. Eng. Mech. Div. ASCE*, **85**, 67-94 (1959).
5. A. Cardona and M. Geradin, 'Time integration of the equations of motion in mechanism analysis', *Comput. Struct.*, **33**, 801-820 (1989).
6. H. M. Hilber, T. J. R. Hughes and R. L. Taylor, 'Improved numerical dissipation for time Integration algorithms in structural dynamics'. *Earthquake Eng. Struct. Dyn.*, **5**, 282-292, (1977).
7. C. Farhat, L. Crivelli and M. Géradin, 'On the spectral stability of time integration algorithms for a class of constrained dynamics problems'. *Proc. 34th Structures, Structural Dynamics, and Materials Conference*, La Jolla, California, 19-22 April, 1993, Paper No AIAA-93-1306-CP.
8. J. C. Simo and K. Wong, 'Unconditionally stable algorithms for rigid body dynamics that exactly preserve energy and momentum'. *Int. j. numer. methods eng.*, **31**, 19-52 (1991).
9. J. C. Simo and N. Tarnow, 'The discrete energy-momentum method. Conserving algorithms for nonlinear dynamics'. *ZAMP*, **43**, 757-792 (1992).
10. E. J. Haug, *Intermediate Dynamics*. Prentice-Hall, Englewood Cliffs, N.J., 1992.
11. J. Chung and G. M. Hulbert, 'A time integration algorithm for structural dynamics with improved numerical dissipation: the generalized- α method', *Journal of Applied Mechanics*, to appear.